Aalto University

Lehtinen, Jyri J.; Käpylä, Maarit J.; Olspert, Nigul; Spada, Federico

A Knee-Point in the Rotation-Activity Scaling of Late-type Stars with a Connection to Dynamo Transitions

A Knee-Point in the Rotation–Activity Scaling of Late-type Stars with a Connection to Dynamo Transitions

Jyri J. Lehtinen,[1] Maarit J. Käpylä,[2, 1, 3] Nigul Olspert,[1] and Federico Spada[1]

[1]Max Planck Institute for Solar System Research, Justus-von-Liebig-Weg 3, D-37077 Göttingen, Germany
[2]Department of Computer Science, Aalto University, PO Box 15400, FI-00076 Aalto, Finland
[3]Nordita, KTH Royal Institute of Technology and Stockholm University, Roslagstullsbacken 23, SE-10691 Stockholm, Sweden

ABSTRACT

The magnetic activity of late-type stars is correlated with their rotation rates. Up to a certain limit, stars with smaller Rossby numbers, defined as the rotation period divided by the convective turnover time, have higher activity. A more detailed look at this rotation–activity relation reveals that, rather than being a simple power law relation, the activity scaling has a shallower slope for the low-Rossby stars than for the high-Rossby ones. We find that, for the chromospheric Ca II H&K activity, this scaling relation is well modelled by a broken two-piece power law. Furthermore, the knee-point of the relation coincides with the axisymmetry to non-axisymmetry transition seen in both the spot activity and surface magnetic field configuration of active stars. We interpret this knee-point as a dynamo transition between dominating axi- and non-axisymmetric dynamo regimes with a different dependence on rotation and discuss this hypothesis in the light of current numerical dynamo models.

1. INTRODUCTION

The magnetic activity of late-type stars is known to be correlated with their rotation rate, faster rotation leading to increased levels of non-thermal emission in the upper stellar atmospheres from the chromosphere to the corona (e.g., Noyes et al. 1984; Vilhu 1984). This scaling is understood to be a consequence of dynamo action in the turbulent outer convective envelopes of the stars, where the efficiency of the magnetic field generation is governed by the rotation and the non-uniformities related to it (see, e.g., Charbonneau 2010), thus leading to different levels of magnetic heating.

The rotation-governed scaling holds for both the observed activity (Noyes et al. 1984; Gilliland 1985; Basri 1987) and magnetic fields (Saar 2001; Aurière et al. 2015; Folsom et al. 2018; Kochukhov et al. 2020) for stars with sufficiently low Rossby numbers, $\mathrm{Ro} = P_{\mathrm{rot}}/\tau_{\mathrm{c}}$, where P_{rot} is the rotation period and τ_{c} the convective turnover time in the stellar convection zone. For faster rotation, both the activity (Vilhu 1984; Pizzolato et al. 2003; Douglas et al. 2014; Astudillo-Defru et al. 2017; Newton et al. 2017; Wright et al. 2018) and magnetic fields

(Reiners et al. 2009; Vidotto et al. 2014; Shulyak et al. 2019) become decoupled from rotation.[1] We will call here the high and low Rossby regimes of the rotation–activity relation as the "rotation-dependent" (RD) and "rotation-independent" (RI) regimes of activity or magnetic field scaling, respectively.

Remarkably, both main sequence and evolved stars, at least in the RD regime, show indications of sharing a similar dynamo process. They follow the same rotation scaling of both activity (Basri 1987; Lehtinen et al. 2020) and magnetic fields (Aurière et al. 2015; Kochukhov et al. 2020) and high activity stars are found both among the main sequence and evolved stars (see Schröder et al. 2018, as well as Figure 1 for the highest chromospheric Ca II H&K fluxes, $\log R'_{\mathrm{HK}} > -4.4$).

---

[1] In observational literature, this is commonly referred to as the "saturation regime" of magnetic activity. In dynamo theory, however, this term is used to refer to the stage of stellar dynamos, where magnetic field, after an initial exponential growth, levels off (saturates) due to the interplay of various nonlinearities. All observed active stars in the main sequence, even those with slow rotation, are in this nonlinear saturation regime.
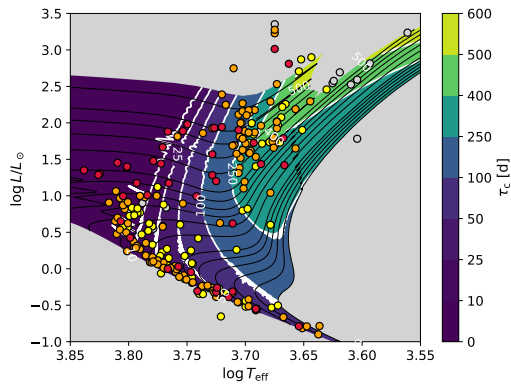
Figure 1. Hertzsprung–Russell diagram of the stellar sample in Lehtinen et al. (2020). Chromospheric activity of the stars is indicated by colour: *red* for $\log R'_{\rm HK} > -4.4$, *orange* for $-4.8 < \log R'_{\rm HK} < -4.4$, *yellow* for $-5.2 < \log R'_{\rm HK} < -4.8$ and *grey* for $\log R'_{\rm HK} < -5.2$. Evolutionary tracks and isocontours of the convective turnover time $\tau_{\rm c}$ are shown for solar metallicity.

Several slowly rotating giants also have distinct activity cycles (Olspert et al. 2018), providing clear evidence of the existence of cyclic dynamos in them.

Already Noyes et al. (1984) and Rutten (1987) noted that, also within the RD regime, the chromospheric rotation–activity relation is shallower for the faster rotators and has a break in its slope at mid-activity levels, around $\log R'_{\rm HK} \approx -4.5$. Noyes et al. (1984) presented both an empirical polynomial and an exponential fit for the relation and speculated on the possible physical causes for its shape. They did not, however, come to a clear conclusion about the interpretation. Since then, the chromospheric activity scaling has most often been modelled by a smooth exponential in the RD regime (Gilliland 1985; Stępień 1994; Kiraga & Stępień 2007; Suárez Mascareño et al. 2016), while some authors have also presented piecewise fits to account for a localised knee in the scaling relation (Mamajek & Hillenbrand 2008; Mittag et al. 2018; Suárez Mascareño et al. 2016). The same curved profile is also visible in the coronal X-ray scaling (Vilhu 1984; Hempelmann et al. 1995; Mamajek & Hillenbrand 2008; Mittag et al. 2018), although this has not been studied in equal detail.

So far there has not been a conclusive interpretation of the shape of the activity scaling relation and none of the published studies present physically motivated justifications for their choice of fitting functions. Theoretically, power law relations, possibly with different exponents in different regimes, are the most naturally expected result from the magnetohydrodynamic (MHD) equations, wherefrom the non-dimensional numbers, like the Rossby number discussed in this study, are derived.[2] A break between two power law segments with different slopes could relate to a transition from one dominating dynamo regime to another one with a different rotation dependence. No similar physical justification is available for the other proposed shapes of the scaling relation.

In this paper we follow on our previous study (Lehtinen et al. 2020) of the chromospheric rotation–activity relation of partially convective main sequence and evolved stars with the aim of establishing a more physically motivated understanding of the observed knee. Our stellar sample covers the RD regime of the activity scaling up to the RD–RI transition, and is thus ideally suited for the study.

2. STELLAR DATA

We use the same stellar data as in Lehtinen et al. (2020), with a few added constraints. The data consist of the time averaged Ca II H&K line core emission to bolometric flux ratios, $R'_{\rm HK} = F'_{\rm HK}/F_{\rm bol}$, and rotation periods, $P_{\rm rot}$, derived for the stars from the Mount Wilson Observatory S-index time series (Wilson 1978). We derived the Rossby numbers using convective turnover times, $\tau_{\rm c}$, estimated using the YaPSI stellar evolution models (Spada et al. 2017). The derivation of these stellar parameters is described in detail in Lehtinen et al. (2020) and the convective turnover times are discussed further in Sect. 3.1.

The subgiants have the most uncertain evolutionary track fits and thus cause considerable scatter in the rotation–activity relation. For this reason, we have excluded them from the current study. We have also excluded all stars with $\tau_{\rm c} < 5$ d, as was done in Lehtinen et al. (2020), since these remain highly uncertain for all stars and are dominated by systematic errors stemming from the stellar structure models. Finally, we excluded four stars with low activity but suspiciously short $P_{\rm rot}$ as having spurious period detections.

Our final sample consists of 54 F- to K-type main sequence stars and 41 giants. We have analysed these separately for the main sequence sample (MS) and the full combined sample (Combined), which includes also the giants. This analysis allows for investigating the effect of the increased scatter from the giants in estimating the shape of the activity scaling relation. We have not analysed the giants as their own separate sample, since their larger scatter and concentration around the mid-activity levels, $-4.8 \lesssim \log R'_{\rm HK} \lesssim -4.4$, means that on

---

[2] Theoretical studies usually prefer the Coriolis number over the Rossby number. These numbers are related to each other via inverse proportionality, $\mathrm{Co} \propto \mathrm{Ro}^{-1}$.
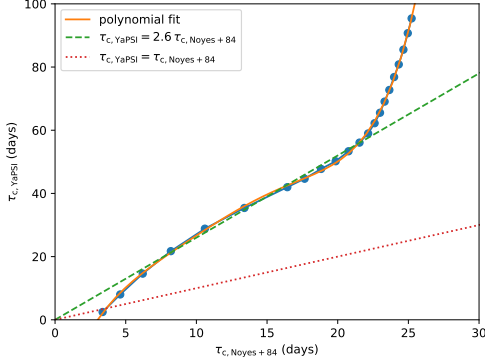
Figure 2. Relation between the convective turnover times, τ_c, derived for main sequence stars from the YaPSI models and the Noyes et al. (1984) empirical formula. The dotted and dashed lines indicate linear identity and $\tau_{c,\mathrm{YaPSI}} = 2.6\,\tau_{c,\mathrm{N84}}$ relations between the two τ_c scales.

their own they contain little information on the shape of the scaling relation.

3. RESULTS

3.1. *Convective turnover times*

The complex relation between the convective turnover time in the stellar outer convective envelope and the location of the star in the Hertzsprung–Russell diagram is illustrated in Figure 1. This shows, for solar metallicity, the isocontours of the turnover time $\tau_{c,\mathrm{YaPSI}}$, derived from the YaPSI stellar evolution models (Spada et al. 2017). There is a steep increase in the turnover times towards the evolved giants, due to their greatly expanded outer layers. Such behaviour is not captured by the more commonly used ways of estimating τ_c, most notably the empirical formula by Noyes et al. (1984), which parameterizes τ_c only for the main sequence as a function of the photometric color $B - V$. In general, for post-main sequence stars, τ_c cannot be expressed as a function of one single parameter.

As the empirical formula of Noyes et al. (1984) has been widely used, we have compared in Figure 2 their $\tau_{c,\mathrm{N84}}$ values with our $\tau_{c,\mathrm{YaPSI}}$. The $\tau_{c,\mathrm{YaPSI}}$ values were extracted from the stellar models at an evolutionary stage approximately halfway through the main sequence, defined as the instant when half of the central hydrogen has been exhausted by nuclear reactions. This choice, rather than a classical isochrone, is more representative of a heterogeneous sample of field stars, such as the ones included in the Mount Wilson catalog.

For a wide range of values ($\tau_{c,\mathrm{YaPSI}} = 18$–$57$ d, and $\tau_{c,\mathrm{N84}} = 7$–$22$ d, respectively, corresponding with late F- to early K-type main sequence stars), the turnover times follow approximately a linear relation, $\tau_{c,\mathrm{YaPSI}} =$

$2.6\,\tau_{c,\mathrm{N84}}$. This approximation breaks down both at low and high τ_c, although the exact relation remains monotonous. For the higher mass main sequence stars, with the shortest τ_c, the $\tau_{c,\mathrm{YaPSI}}$ values quickly drop to zero as the outer convective envelope becomes shallower and disappears. For the low mass stars with the longest τ_c, the empirical $\tau_{c,\mathrm{N84}}$ fails to fully capture the steep increase, predicted by the models.

The relation between $\tau_{c,\mathrm{YaPSI}}$ and $\tau_{c,\mathrm{N84}}$ can be satisfactorily represented by a fifth-order polynomial fit,

$$
\begin{aligned}
\tau_{c,\mathrm{YaPSI}} = & -30.7 + 15.2\tau_{c,\mathrm{N84}} \\
& - 2.16\tau_{c,\mathrm{N84}}^2 + 0.192\tau_{c,\mathrm{N84}}^3 \\
& - 0.00839\tau_{c,\mathrm{N84}}^4 + 0.000141\tau_{c,\mathrm{N84}}^5.
\end{aligned} \tag{1}
$$

This relation, naturally, does not apply for the evolved stars, as $\tau_{c,\mathrm{N84}}$ is not defined for them.

3.2. *Two-piece power law model*

We modelled the shape of the observed R'_{HK} vs. Ro rotation–activity relation using a two-piece power law model. This offers the most physically motivated description of the activity scaling, as discussed in the Introduction, and allows locating a precise knee-point for the scaling law, that can be compared with other results.

Our regression model is

$$
R'_{\mathrm{HK}}(\mathrm{Ro}) = f(\mathrm{Ro}) = \begin{cases} C_1\,\mathrm{Ro}^{\beta_1}, & \mathrm{Ro} \leq \mathrm{Ro}_0 \\ C_2\,\mathrm{Ro}^{\beta_2}, & \mathrm{Ro} > \mathrm{Ro}_0, \end{cases} \tag{2}
$$

where $C_2 = C_1\,\mathrm{Ro}_0^{\beta_1 - \beta_2}$, ensuring continuity at the knee-point, $\mathrm{Ro} = \mathrm{Ro}_0$. We assumed that the observed uncertainties of $\log R'_{\mathrm{HK}}$ follow a normal distribution, leading to a log-normal likelihood function for R'_{HK},

$$
p(R'_{\mathrm{HK}}|\mu, \sigma^2) = \log\text{-Normal}(R'_{\mathrm{HK}}|f(\mathrm{Ro}), \sigma^2), \tag{3}
$$

where the mean, μ, is given by the regression model $f(\mathrm{Ro})$ and the scale by the scatter parameter σ. This analysis is similar to that of Douglas et al. (2014), Newton et al. (2017) and Wright et al. (2018) with the exception that our model does not cover the RI regime, but has instead separate power law exponents $\beta_{\{1,2\}}$ on the opposite sides of Ro_0. A description of our regression procedure, using Markov Chain Monte Carlo with the `emcee` Python package (Foreman-Mackey et al. 2013), is given in the Appendix (Sect. A).

In Table 1 we list the parameter estimates of the model fits done for the MS and Combined samples, including derived estimates for the knee-point location as Ro_0 and $\log R'_{\mathrm{HK},0} = \log f(\mathrm{Ro}_0)$. We have also calculated rough estimates for the knee-point Rossby number in the Noyes

Table 1. Fit coefficients of the power law model for the MS and Combined samples

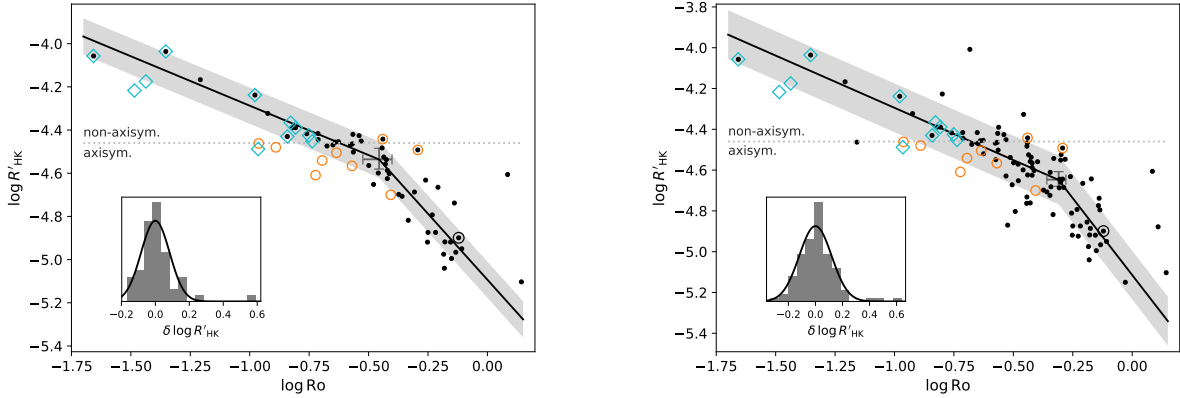|	$\log C_1$	β_1	β_2	$\log \mathrm{Ro}_0$	σ	$\log R'_{\mathrm{HK},0}$	Ro_0	$\mathrm{Ro}_{0,\mathrm{N84}}$
MS	$-4.745^{+0.051}_{-0.047}$	$-0.458^{+0.062}_{-0.061}$	$-1.222^{+0.146}_{-0.181}$	$-0.456^{+0.054}_{-0.068}$	$0.084^{+0.009}_{-0.008}$	$-4.536^{+0.051}_{-0.045}$	$0.350^{+0.047}_{-0.051}$	0.91
Combined	$-4.807^{+0.038}_{-0.036}$	$-0.512^{+0.059}_{-0.059}$	$-1.507^{+0.279}_{-0.293}$	$-0.310^{+0.030}_{-0.050}$	$0.119^{+0.010}_{-0.008}$	$-4.647^{+0.039}_{-0.033}$	$0.490^{+0.036}_{-0.053}$	1.3

Figure 3. Two-piece power law fits to the R'_{HK} vs. Ro rotation–activity relation of the MS (left panel) and Combined (right panel) samples. The light grey shaded area marks the $\pm 1\sigma$ range of the likelihood function and the error bars at the knee-point indicate the uncertainty in its location. The orange circles and cyan diamonds denote stars that Lehtinen et al. (2016) found to have axisymmetric or non-axisymmetric spot distributions, respectively, and the horizontal dotted lines mark the identified transition between these regimes. Insets show the $\delta \log R'_{\mathrm{HK}}$ residual distributions and the corresponding likelihood function profiles. The Sun is indicated as the black circled dot.

et al. (1984) scale, $\mathrm{Ro}_{0,\mathrm{N84}}$, to aid comparison with other published studies. These values were calculated from our Ro_0 values in the YaPSI scale, using the approximate linear relation $\tau_{\mathrm{c,YaPSI}} = 2.6\,\tau_{\mathrm{c,N84}}$. A more accurate rescaling is not feasible, since the nonlinear relation between the two τ_{c} scales (Eq. 1) does not directly translate for the Rossby numbers, which also depend on P_{rot}. For the same reason we also do not attempt to derive accurate error estimates for $\mathrm{Ro}_{0,\mathrm{N84}}$.

The regression fits for the MS and Combined samples are shown in Figure 3. They show general agreement with each other, although the Combined sample has increased scatter from the giants around the knee-point, which has pushed its Ro_0 towards larger values. We find, nevertheless, that the better defined MS sample places the knee close to the $\log R'_{\mathrm{HK}} = -4.46$ limit where Lehtinen et al. (2016) found a sharp transition between axisymmetric and non-axisymmetric spot activity, surfacing as long-lived active longitudes. This suggests that the onset of non-axisymmetry and the break in the activity scaling slope may be related phenomena.

Further evidence supporting this claim is provided by a comparison with See et al. (2016). They studied the magnetic topologies of a sizable sample of ac-

tive stars from Zeeman Doppler imaging inversions and found a transition from mostly poloidal axisymmetric fields to mostly toroidal non-axisymmetric fields, occurring around their Ro = 1. Their Rossby numbers were based on a τ_{c} scale closely related to Noyes et al. (1984), so their transition line can be compared with our $\mathrm{Ro}_{0,\mathrm{N84}}$. Their axisymmetric to non-axisymmetric transition falls thus close to the knee-point in both our MS and Combined samples.

Insets in Figure 3 show the residuals of $\log R'_{\mathrm{HK}}$ against the regression model,

$$\delta \log R'_{\mathrm{HK}} = \log R'_{\mathrm{HK}} - \log f(\mathrm{Ro}). \quad (4)$$

These are in both cases in good agreement with the profiles of the log-normal likelihood function (Eq. 3).

Finally, we tested the validity of the two-piece power law model against the often used exponential model,

$$R'_{\mathrm{HK}}(\mathrm{Ro}) = C e^{\beta \mathrm{Ro}}, \quad (5)$$

using the same likelihood function (Eq. 3). To compare the two models, we calculated the values of their relative Bayesian information criterion (BIC, Stoica & Selen 2004),

$$\Delta \mathrm{BIC} = \mathrm{BIC}(\text{power law}) - \mathrm{BIC}(\text{exponential}). \quad (6)$$

For the MS sample we found ΔBIC $= -2.89$, meaning that the two-piece power law model minimizes the BIC and provides a better model for the data. For the Combined sample we find the opposite to be true, ΔBIC $= 3.52$, which would favour the exponential model instead. This may be attributed to the larger scatter of the Combined sample, which makes the knee-point less defined. We claim here that the power law behavior is more physical and that the preference for an exponential model in the Combined sample results from the higher uncertainty in determining τ_c for the evolved stars (Lehtinen et al. 2020).

3.3. Gaussian clustering model

To get a statistically independent look at the data, we also applied a Gaussian mixture model with expectation maximisation algorithm (Barber 2012) for both the MS and Combined samples. We tested models with a number of clusters from one to five and determined the best model by minimizing their BIC.

The clustering results are shown in Figure 4. For both the MS and Combined samples the data are best described by a bimodal model with two clusters intersecting at the the knee-point. This hints at an abrupt change in the scaling relation, inconsistent with a smooth exponential model. Note that in Lehtinen et al. (2020) we found a single Gaussian cluster for the whole RD regime and a surrounding outlier cluster, using the same algorithm. In the current study we have excluded the obvious outliers from the sample, explaining the improved ability of the clustering to model the shape of the activity scaling.

Figure 4 also includes the regression fits for the two samples. Notably, both for the MS and Combined samples, the two clusters intersect close to the knee in the MS sample fit. The clustering seems thus unaffected by the increased scatter in the Combined sample. We may then conclude that the MS fit gives a more robust model of the activity scaling, even for the full Combined sample, which provides additional evidence for relating the knee with the axi- to non-axisymmetric transition.

4. DISCUSSION

To fully understand the different activity levels in different types of stars, one would need to understand both how stellar dynamos depend on rotational properties and how their nonlinear saturation mechanism works. The latter is especially problematic for the following reasons. In mean-field dynamo models, very often, an ad hoc quenching formula is used, utilizing the assumption that the growing magnetic field starts influencing the flow field when the magnetic energy reaches equiparti-

tion with the kinetic energy of the flow (see e.g. Charbonneau 2010, and references therein). Such an approach does not help in understanding how the saturation process occurs. There are also more physical attempts to use the magnetic helicity conservation law to derive a dynamic equation for the α effect (see e.g. Brandenburg & Subramanian 2005, and references therein). In this case the saturation level becomes dependent on various additional physical parameters, such as the magnetic Reynolds number, and the helicity fluxes out of the dynamo active domain. Unfortunately, these parameters are largely unknown, and in practice this approach only increases the number of unknowns in the problem.

Hence, the only remaining route are the so called direct numerical simulations where the full set of MHD equations is solved. This retains the Lorentz force feedback and allows for the magnetic helicity fluxes, that are thought to be vital in the nonlinear saturation process. The problem with this approach is that these models are still far removed from the realistic parameter regime of stars; most notably the viscosity, resistivity and thermal conduction being far increased from the real objects. There are some works that have already studied the rotation dependence of the dynamo solutions either in axisymmetric wedges (Käpylä et al. 2013, 2017; Warnecke 2018; Warnecke & Käpylä 2019), latitudinal wedges covering the full longitudinal extent (Viviani et al. 2018; Viviani & Käpylä 2020), or in full spheres (Nelson et al. 2013; Strugarek et al. 2017). In such models the axi- to non-axisymmetric transition is seen (e.g. Viviani et al. 2018, but requiring high enough resolution), lending support to connecting the observed knee with this transition. The transition point is, however, located still at too low rotation rates in comparison to observations. Recently, Viviani & Käpylä (2020) have shown that an improved description of the heat conduction used in the model can push the transition into a more realistic direction.

The increase of the magnetic energy in the models as a function of rotation is also not correctly captured, unless the magnetic energy is normalized with the kinetic energy (see e.g. Viviani et al. 2018; Warnecke 2018; Warnecke & Käpylä 2019). In this case the normalized energy is seen increasing roughly proportional to the Coriolis number, in rough agreement with the observations. However, no such knee-point, as observationally confirmed, can be seen in these simulations. On the contrary, the increase of the magnetic to kinetic energy ratio occurs smoothly over the axi-to non-axisymmetric dynamo mode transition. These discrepancies could indicate that the models do not yet take correctly into account the rotational dependence of the critical Rayleigh
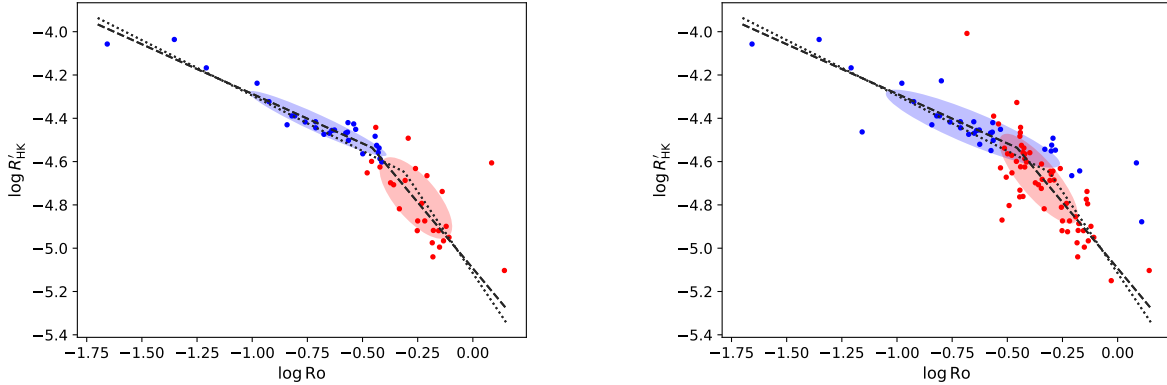
Figure 4. Optimal Gaussian clustering for the MS (left panel) and Combined (right panel) samples. The clusters are denoted by the blue and red ellipses and their inferred members with corresponding colors. The regression fits of the MS (dashed line) and Combined samples (dotted line) are shown on top of the clusters.

number for the onset of convection: the more rapid the rotation, the harder convection becomes to excite. Unless the thermal conduction is decreased correspondingly when rotation rate is increased, which is usually not done in the modelling attempts, the energy in the convective motions might become underestimated in the rapidly rotating cases.

5. CONCLUSIONS

Our results provide strong evidence of the rotation–activity relation not being smooth in the rotation-dependent regime but rather having a localized break at mid-activity levels. For the main sequence stars, a two-piece power law model, with distinctly different slopes on either sides of this knee-point, clearly describes the activity data better than an often-used, smooth, exponential model. According to our model fit comparison, including giant stars in the sample would make the exponential model the preferred one. Our Gaussian clustering analysis, however, finds the knee-point regardless of whether the giant stars are considered or not. Since power law relations are also physically expected to arise from the MHD equations, unlike exponential ones, we conclude the two-piece power law model to be a more accurate description of the activity scaling relation.

We argue that the break in the activity scaling can be interpreted as a transition between two dynamo regimes, dominating at different rotation rates. A good candidate for identifying with this transition is the shift from axi- to non-axisymmetric magnetic configurations, as this transition has been observed to occur at nearly the same activity levels and Rossby numbers for both spot activity (Lehtinen et al. 2016) and surface magnetic fields (See et al. 2016) as we find here for the knee-point.

REFERENCES

Astudillo-Defru, N., Delfosse, X., Bonfils, X., et al. 2017, A&A, 600, A13

Aurière, M., Konstantinova-Antova, R., Charbonnel, C., et al. 2015, A&A, 574, A90

Barber, D. 2012, Bayesian Reasoning and Machine Learning (Cambridge University Press)

Basri, G. 1987, ApJ, 316, 377

Brandenburg, A., & Subramanian, K. 2005, PhR, 417, 1

Charbonneau, P. 2010, Liv. Rev. Sol. Phys., 7, 3

Douglas, S. T., Agüeros, M. A., Covey, K. R., et al. 2014, ApJ, 795, 161

Folsom, C. P., Bouvier, J., Petit, P., et al. 2018, MNRAS, 474, 4956

Foreman-Mackey, D., Hogg, D. W., Lang, D., & Goodman, J. 2013, PASP, 125, 306

Gilliland, R. L. 1985, ApJ, 299, 286

Goodman, J., & Weare, J. 2010, Communications in Applied Mathematics and Computational Science, 5, 65

Hempelmann, A., Schmitt, J. H. M. M., Schultz, M., Ruediger, G., & Stepien, K. 1995, A&A, 294, 515

Käpylä, P. J., Käpylä, M. J., Olspert, N., Warnecke, J., & Brandenburg, A. 2017, A&A, 599, A4

Käpylä, P. J., Mantere, M. J., Cole, E., Warnecke, J., & Brandenburg, A. 2013, ApJ, 778, 41

Kiraga, M., & Stępień, K. 2007, AcA, 57, 149

Kochukhov, O., Hackman, T., Lehtinen, J. J., & Wehrhahn, A. 2020, A&A, 635, A142

Lehtinen, J., Jetsu, L., Hackman, T., Kajatkari, P., & Henry, G. W. 2016, A&A, 588, A38

Lehtinen, J. J., Spada, F., Käpylä, M. J., Olspert, N., & Käpylä, P. J. 2020, Nature Astronomy, doi: 10.1038/s41550-020-1039-x

Mamajek, E. E., & Hillenbrand, L. A. 2008, ApJ, 687, 1264

Mittag, M., Schmitt, J. H. M. M., & Schröder, K. P. 2018, A&A, 618, A48

Nelson, N. J., Brown, B. P., Brun, A. S., Miesch, M. S., & Toomre, J. 2013, ApJ, 762, 73

Newton, E. R., Irwin, J., Charbonneau, D., et al. 2017, ApJ, 834, 85

Noyes, R. W., Hartmann, L. W., Baliunas, S. L., Duncan, D. K., & Vaughan, A. H. 1984, ApJ, 279, 763

Olspert, N., Lehtinen, J. J., Käpylä, M. J., Pelt, J., & Grigorievskiy, A. 2018, A&A, 619, A6

Pizzolato, N., Maggio, A., Micela, G., Sciortino, S., & Ventura, P. 2003, A&A, 397, 147

Reiners, A., Basri, G., & Browning, M. 2009, ApJ, 692, 538

Rutten, R. G. M. 1987, A&A, 177, 131

Saar, S. H. 2001, in Astronomical Society of the Pacific Conference Series, Vol. 223, 11th Cambridge Workshop on Cool Stars, Stellar Systems and the Sun, ed. R. J. Garcia Lopez, R. Rebolo, & M. R. Zapaterio Osorio, 292

Schröder, K. P., Schmitt, J. H. M. M., Mittag, M., Gómez Trejo, V., & Jack, D. 2018, MNRAS, 480, 2137

See, V., Jardine, M., Vidotto, A. A., et al. 2016, MNRAS, 462, 4442

Shulyak, D., Reiners, A., Nagel, E., et al. 2019, A&A, 626, A86

Spada, F., Demarque, P., Kim, Y.-C., Boyajian, T. S., & Brewer, J. M. 2017, Astrophys. J., 838, 161

Stępień, K. 1994, A&A, 292, 191

Stoica, P., & Selen, Y. 2004, IEEE Signal Processing Magazine, 21, 36

Strugarek, A., Beaudoin, P., Charbonneau, P., Brun, A. S., & do Nascimento, J.-D. 2017, Science, 357, 185

Suárez Mascareño, A., Rebolo, R., & González Hernández, J. I. 2016, A&A, 595, A12

Vidotto, A. A., Gregory, S. G., Jardine, M., et al. 2014, MNRAS, 441, 2361

Vilhu, O. 1984, in ESA Special Publication, Vol. 218, Fourth European IUE Conference, ed. E. Rolfe, 239–242

Viviani, M., & Käpylä, M. J. 2020, arXiv e-prints, arXiv:2006.04426. https://arxiv.org/abs/2006.04426

Viviani, M., Warnecke, J., Käpylä, M. J., et al. 2018, A&A, 616, A160

Warnecke, J. 2018, A&A, 616, A72

Warnecke, J., & Käpylä, M. J. 2019, arXiv e-prints, arXiv:1910.06776. https://arxiv.org/abs/1910.06776

Wilson, O. C. 1978, Astrophys. J., 226, 379

Wright, N. J., Newton, E. R., Williams, P. K. G., Drake, J. J., & Yadav, R. K. 2018, MNRAS, 479, 2351
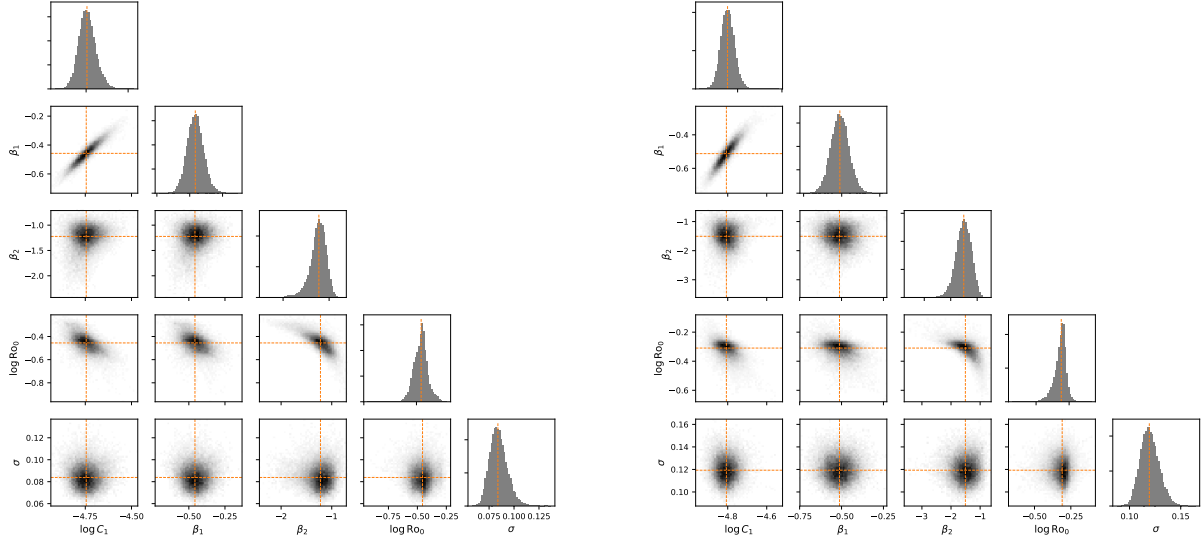
Figure 5. The posterior distributions of the two-piece power law model parameters for the MS sample (left panel) and the Combined sample (right panel). The median estimates of each parameter are marked with the orange dashed lines.

APPENDIX

A. THE MCMC REGRESSION

We performed the regression of the two-piece power law model, defined by Eqs. 2 and 3, by treating $\log C_1$, β_1, β_2, $\log \mathrm{Ro_0}$, and σ as the independent free model parameters and sampling their joint posterior distribution. We used the `emcee` Python package (Foreman-Mackey et al. 2013), which implements an affine invariant Markov Chain Monte Carlo (MCMC) ensemble sampler (Goodman & Weare 2010). As the priors, we used weakly informative Gaussian priors $p(\beta) = \mathcal{N}(\beta \mid -1, 1^2)$ and $p(\log \mathrm{Ro_0}) = \mathcal{N}(\log \mathrm{Ro_0} \mid -0.5, 0.25^2)$ for $\beta_{\{1,2\}}$ and $\log \mathrm{Ro_0}$, a non-informative Jeffreys prior $p(\sigma^2) = 1/\sigma^2$ for σ and a uniform prior for $\log C_1$. The $\beta_{\{1,2\}}$ and $\log \mathrm{Ro_0}$ priors were chosen to specify a negative slope for the fit and a rough knee-point location based on visual inspection of the data. In addition, we discarded stars with Ro > 1 from the fit, since this range is dominated by scattered outliers (see further discussion in Lehtinen et al. 2020).

We set up the MCMC sampler to run with 100 chains of 2000 iterations and removed the first half of each chain to ensure good convergence. The parameter estimates and their error bars, reported in Table 1, were calculated as the median values and the 16th and 84th percentiles of the sampled Markov chains. The full posterior distributions for the MS and Combined samples are shown in Figure 5, including histograms of the marginal distributions of each model parameter.

For the smooth exponential model (Eq. 5) the parameter estimates are $\log C = -4.177^{+0.027}_{-0.027}$, $\beta = -1.065^{+0.062}_{-0.061}$ and $\sigma = 0.091^{+0.010}_{-0.008}$ for the MS sample and $\log C = -4.214^{+0.028}_{-0.029}$, $\beta = -0.968^{+0.067}_{-0.065}$ and $\sigma = 0.121^{+0.009}_{-0.008}$ for the Combined sample.